

## Article

# A Simulated Investigation of Lithium Niobate Orientation Effects on Standing Acoustic Waves

Ranjith D. Janardhana <sup>1</sup> and Nathan Jackson <sup>1,2,\*</sup> <sup>1</sup> Department of Mechanical Engineering, University of New Mexico, Albuquerque, NM 87131, USA<sup>2</sup> Nanoscience and Microsystems Engineering, University of New Mexico, Albuquerque, NM 87131, USA

\* Correspondence: njack@unm.edu

**Abstract:** The integration of high-frequency acoustic waves with microfluidics has been gaining popularity as a method of separating cells/particles. A standing surface acoustic wave (sSAW) device produces constructive interference of the stationary waves, demonstrating an increase in cell separating efficiency without damaging/altering the cell structure. The performance of an sSAW device depends on the applied input signal, design of the IDT, and piezoelectric properties of the substrate. This work analyzes the characteristics of a validated 3D finite element model (FEM) of LiNbO<sub>3</sub> and the effect on the displacement components of the mechanical waves under the influence of sSAWs by considering XY-, YX-, and 128° YX-cut LiNbO<sub>3</sub> with varying electrode length design. We demonstrated that device performance can be enhanced by the interference of multiple waves under a combination of input signals. The results suggest that 128° YX-cut LiNbO<sub>3</sub> is suitable for generating higher-amplitude out-of-plane waves which can improve the effectiveness of acoustofluidics-based cell separation. Additionally, the findings showed that the length of the electrode impacts the formation of the wavefront significantly.

**Keywords:** standing acoustic waves; acoustofluidics; cell separation; microelectromechanical systems; FEM; SAW



**Citation:** Janardhana, R.D.; Jackson, N. A Simulated Investigation of Lithium Niobate Orientation Effects on Standing Acoustic Waves. *Sensors* **2023**, *23*, 8317. <https://doi.org/10.3390/s23198317>

Academic Editor: Yupan Wu

Received: 5 September 2023

Revised: 3 October 2023

Accepted: 6 October 2023

Published: 8 October 2023



**Copyright:** © 2023 by the authors. Licensee MDPI, Basel, Switzerland. This article is an open access article distributed under the terms and conditions of the Creative Commons Attribution (CC BY) license (<https://creativecommons.org/licenses/by/4.0/>).

## 1. Introduction

Acoustofluidics is an emerging field of research that combines acoustics with microfluidics. Acoustofluidics can be used in a wide range of applications, including particle separation, micro-mixing, channel sorting, bubble formation, and atomization, all of which involve particle or fluid manipulation due to acoustic waves [1]. The common application of acoustofluidics is in the areas of cell sorting, particle separation, fluid mixing, and atomization and involves the creation of out-of-plane surface waves using a surface acoustic wave (SAW) device that interacts with fluid media. There have been significant advances in using acoustofluidics in particle separation and in understanding the mechanism of action, which includes energy transmission from acoustic waves, flow of the liquid, wave transmission through microfluidic channels, and acoustic radiation force. These high-propagating mechanical waves are a combination of planar and transverse waves that operate at higher frequencies (100 s of MHz) and decay along the depth of the piezoelectric substrate [2–5]. The frequency of the waves is dependent on the acoustic velocity of the piezoelectric material and wavelength which is determined by the width and spacing of the interdigitated transducers (IDTs) or electrodes. Basic SAW devices are relatively easy to fabricate as they consist of a piezoelectric substrate and an electrically conducting IDT. More complicated structures could include coatings, reflectors, and phononic crystals to guide the waves. A voltage applied to the IDT produces a traveling SAW (tSAW) through the piezoelectric material. Due to the anisotropic features of the piezoelectric material, the wave formation is dependent on the crystal cut of the material, which affects the acoustic velocity and amplitude components [6].

When SAW devices are integrated with a microfluidic channel consisting of a liquid medium with cells or particles, the propagating waves can be used to separate particles based on size. According to the cell properties such as size, density, and compressibility, the acoustofluidics-based cell separation is the only effective contactless technique that can separate cells without altering or damaging the cells [7,8]. The suspended particles in the microfluidic channel undergo separation due to the predominance of the acoustic radiation force as well as acoustic streaming acting on the particles. The performance of these acoustofluidics methods depends heavily on the performance of the SAW device, being influenced by key factors such as wavefront propagation, operating frequency, displacement components of waves, and IDT design [9–11]. Recent experimental research work on standing SAWs (sSAWs) has demonstrated an improvement in particle/cell separation efficiency [12–16]. Numerical simulation analysis illustrated that the interference of the standing wave increased the out-of-plane amplitude of the waves, which improved the separation of cells/particles due to an increase in acoustic energy. Also, the length of the IDT affects the cell separation [8,17–20]. Therefore, increasing the acoustic energy of the SAW could result in enhanced particle separation capabilities.

Despite extensive experimental work establishing the phenomena, the modeling and simulation of acoustofluidics regarding cell/particle sorting are limited. There has been minimal research conducted by considering the high aspect ratio of length to width of the IDT to investigate the effects of SAW design based on performance. In this regard, this paper explores the characteristics and interference of stationary waves of sSAW devices and considers the higher aspect ratio of length to width of a LiNbO<sub>3</sub> IDT using a finite element model (FEM) in COMSOL Multiphysics commercial software [21]. The goal of this work is to facilitate the acoustic energy along the microfluidic channel by increasing the out-of-plane displacement of the waves by considering the longer length of the IDT design and sSAWs. Initially, the FEM of three-dimensional (3D) X-cut Y-propagating LiNbO<sub>3</sub> consisting of an IDT length of 4500 μm was validated against experimental and simulation results based on the performance factor “Insertion Loss” (IL). The effect of parameters such as the thickness of the IDT and impulse properties were studied. After validating the FEM model, this study further investigates the characteristics of the X-cut Y-propagating LiNbO<sub>3</sub> 3D model. This article also analyzes the impact of sSAWs on stationary wave amplitude under different input signal conditions using three different cuts of LiNbO<sub>3</sub>: 3D XY LiNbO<sub>3</sub>, 3D YX LiNbO<sub>3</sub>, and 3D 128° YX LiNbO<sub>3</sub>. We also investigated the displacement characteristics caused by combining multiple waves. The FEM developed could be useful for researchers interested in enhancing the performance of acoustofluidic devices and could be integrated into a more complex model involving microfluidics in the future.

## 2. Materials and Methods

### 2.1. Model Equation

The constitutive equation for a piezoelectric material that relates electric field and strain [22] is given by

$$T_{ij} = C_{ijkl} S_{kl} - e_{kij} E_k, \quad (1)$$

$$D_i = e_{ikl} S_{kl} + \epsilon_{ik} E_k. \quad (2)$$

where  $T$  refers to the stress tensor,  $S$  indicates the strain tensor,  $S_{ij} = \frac{1}{2} \left( \frac{\partial u_i}{\partial x_j} + \frac{\partial u_j}{\partial x_i} \right)$ ,  $e$  is the piezoelectric constant, and  $D$  is electric displacement. The elastic stiffness matrix, electrical field vector, and permittivity matrix are indicated by  $C$ ,  $E$ , and  $\epsilon$  respectively.

The wave equation [23] in the piezoelectric material is expressed as

$$\frac{\partial T_{ij}}{\partial x_j} = \rho \frac{\partial^2 u_i}{\partial t^2}. \quad (3)$$

where  $\rho$  refers to the density of mass and  $u_i$  are displacement components. The electric field was approximated as quasi-static, and the electric charge was considered to be zero [23,24]. Maxwell's equation becomes

$$E_i = -\frac{\partial V}{\partial x_i}, \quad (4)$$

$$\frac{\partial D_i}{\partial x_i} = 0 \quad (5)$$

where  $V$  indicates electric potential. Further, the piezoelectric constitutive relation is reduced to coupled wave equations by solving Equations (1)–(5) as follows,

$$-\rho \frac{\partial^2 u_i}{\partial t^2} + C_{ijkl} \frac{\partial^2 u_k}{\partial x_j \partial x_l} + e_{kij} \frac{\partial^2 V}{\partial x_k \partial x_j} = 0, \quad (6)$$

$$e_{ikl} \frac{\partial^2 u_k}{\partial x_i \partial x_l} - \epsilon_{ik} \frac{\partial^2 V}{\partial x_i \partial x_k} = 0. \quad (7)$$

with three degrees of freedom for displacement ( $u_i$ ) and one for electric potential ( $V$ ). The convergence error was calculated using  $L_2$  norm [25] on the domain  $\Omega = (a, b)$  and given by

$$\|u - u_h\|_{L_2} = \left( \int_a^b |u - u_h|^2 dx \right)^{\frac{1}{2}}. \quad (8)$$

where  $u$  is considered as reference coarse mesh and  $u_h$  is a finer mesh.  $h$  stands for the length of an element.

## 2.2. Computational Domain

### 2.2.1. Two-Dimensional Domain

The 2D computational model of XY LiNbO<sub>3</sub> used for the verification study is represented in Figure 1. A LiNbO<sub>3</sub> substrate with dimensions of 1600  $\mu\text{m} \times 500 \mu\text{m}$  was used in the initial study. The input and output ports consisted of two-finger pairs of aluminum IDTs with dimensions of 0.3  $\mu\text{m}$  thick and 10  $\mu\text{m}$  wide with a pitch of 10  $\mu\text{m}$ . The input and output IDTs were named "1", "2", "3", and "4" as well as "a", "b", "c", and "d". The chosen periodicity of IDTs was 10  $\mu\text{m}$  ( $\lambda/4$ ) where the wavelength ( $\lambda$ ) was equal to 40  $\mu\text{m}$ . The active area for the microfluidic channel was between the input and output IDTs with a width of 90  $\mu\text{m}$ . The aforementioned computational domain was based on the previously published report [26].

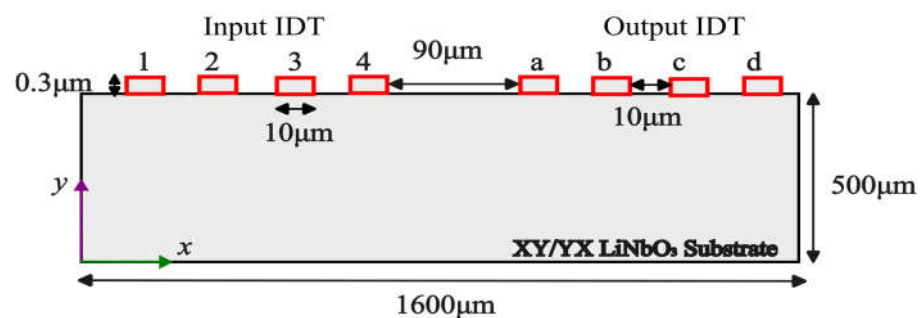


**Figure 1.** Two-dimensional computational domain for SAW device.

### 2.2.2. Three-Dimensional Domain

The 3D computational domain chosen was similar to the 2D domain with overall dimensions 1600  $\mu\text{m} \times 500 \mu\text{m} \times 4700 \mu\text{m}$  as depicted in Figure 2. The longer length of the electrode of 4500  $\mu\text{m}$  was selected, with a thickness and width of 0.3  $\mu\text{m}$  and 10  $\mu\text{m}$ , respectively. The reason for selecting a higher length-to-width aspect ratio was to study the wave formation and reduce the amplitude along the length of the electrode, along with

creating a near  $50 \Omega$  resistance needed for impedance matching. Here the input IDT and output IDT are also referred to as the left and right IDTs, respectively. All other dimensions remained identical to the 2D domain. The total active area under the influence of acoustic waves was  $90 \mu\text{m} \times 4500 \mu\text{m}$ .

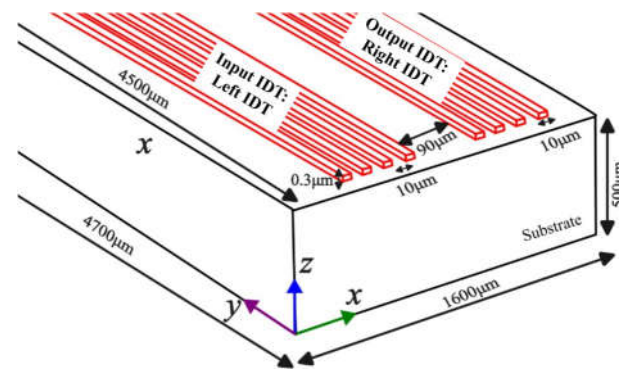


**Figure 2.** Three-dimensional computational domain for SAW device.

### 2.2.3. Mesh and Boundary Conditions

An example of the 2D computational mesh with a zoomed view of area “A” close to IDT is shown in Figure 3a,b. The finer mesh was applied near the surface of the IDT to capture the surface wave utilizing quadrilateral mesh. Also, the finer mesh was used in a region, “block 3”, which consists of active area and IDT as represented in Figure 3. The 2D mesh details are provided in Table 1. A similar finer mesh was utilized for the 3D domain by keeping 40 elements per wavelength near the IDT.

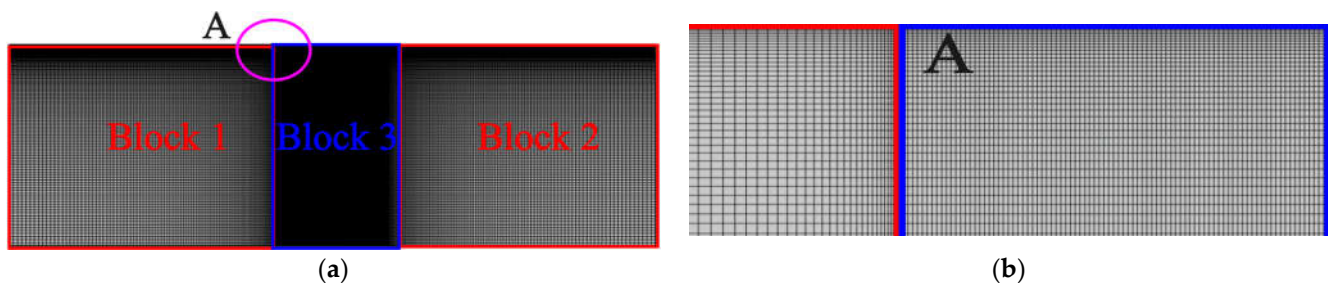


**Figure 3.** Mesh for the (a) 2D SAW device; (b) zoomed view of area “A” near IDT.

**Table 1.** Mesh details for 2D domain.

	Total Number of Elements (N)	Number of Elements Per Wavelength ( $\lambda$ )
Case 1	31,540	20
Case 2	60,080	40
Case 3	88,910	80
Case 4	146,570	160
Case 5	204,230	240

The left and right sides of the 2D domain were enforced with periodic boundary conditions whereas the bottom of the domain was kept fixed. All four sides were applied with periodic boundary conditions, and the bottom part was applied with fixed conditions in the case of the 3D domain. The following impulse signal ( $V_i$ ) was applied at the input IDT as an initial condition for the verification and validation study. The impulse function was applied to the IDT fingers “2” and “4”, and “1” and “3” (Figure 1) were set to ground. Step Pulse [27]:

$$V_i = \begin{cases} 1 \text{ V}, & 0 \leq t \leq 1 \text{ ns.} \\ 0, & t \geq 1 \text{ ns.} \end{cases} \quad (9)$$

A peak-to-peak sinusoidal voltage of 1 V with a frequency of 100 MHz was applied at the input IDT for characteristic analysis of 3D XY LiNbO<sub>3</sub> (section: 3D model). To determine open circuit voltage, the output IDT was configured for the floating potential condition [27]. However, for sSAW case studies, the input signal was applied to both the left and right IDTs (Figure 2) to investigate the effects of combining waves. Table 2 lists the material properties of the IDTs.

**Table 2.** Material properties of IDTs.

Property	Aluminum (IDT)
Young's Modulus (kPa)	$70 \times 10^9$
Poisson's ratio	0.33
Density (kg/m <sup>3</sup> )	2700

#### 2.2.4. Crystal Orientation

Due to the anisotropic characteristics of LiNbO<sub>3</sub>, different orientations of the cut with respect to the crystallographic axes affect material properties such as the elastic stiffness matrix (C), piezoelectric constant (e), acoustic velocity, and permittivity matrix (ε). In COMSOL Multiphysics, crystal cut was applied by rotating the coordinate system based on Euler angles. COMSOL Multiphysics documentation [28] contains further detailed explanations for implementing the material orientation. XY-cut LiNbO<sub>3</sub> indicates that the surface wave propagates in the Y direction normal to the X and Z surface [29]. Correspondingly, YX-cut LiNbO<sub>3</sub> refers to the surface wave generated in the X direction that was normal to the Y and Z direction. Euler angle was set to (0, −90, −90) for XY cut LiNbO<sub>3</sub> for rotating the coordinate system in COMSOL whereas the (0, 90, 0) was applied for YX cut LiNbO<sub>3</sub>. 128° Y cut X propagation Euler angle was set to (0, −38, 0) [7] in COMSOL. Crystal orientation for the LiNbO<sub>3</sub> cuts is depicted in the appendix section (Appendix A).

#### 2.2.5. Numerical Simulation

Numerical simulation was set up according to a previous study [11] that extended the simulation to a 3D model case. COMSOL Multiphysics was used for solving the wave equation (Equations (6) and (7)). The frequency response of the system was analyzed using time-dependent simulation with a time step of 0.1 ns with a total simulation time of 100 ns. This time dependent simulation parameters were similar to previous investigations [11]. Step pulse ( $V_i$ ) mentioned in Equation (9) was applied at the input IDT and the impulse response of the device was recorded at the output IDT. Fast Fourier Transform (FFT) [26] was implemented to acquire the SAW device's frequency response by using "Time to Frequency FFT" option in COMSOL. IL was determined using the following expression [30].

$$IL = 20 \log \left| \frac{V_{output}}{V_i} \right| \quad (10)$$

In contrast, the shape order of the displacement variables was set as quadratic serendipity while electric potential as quadratic to reduce computational time. The default values of COMSOL were used for other solver parameters.

### 3. Results and Discussion

#### 3.1. Validation of a Model

IL is calculated by using Equation (10) with time step = 0.1 ns with a total simulation time of 100 ns and impulse condition from Equation (9). The results are represented in Figure 4a for different cases (Table 1). The normalized error was calculated for 2D XY

LiNbO<sub>3</sub> at various frequencies using the L<sub>2</sub> norm (Equation (8)) with respect to different total number of elements as shown in Figure 4b.

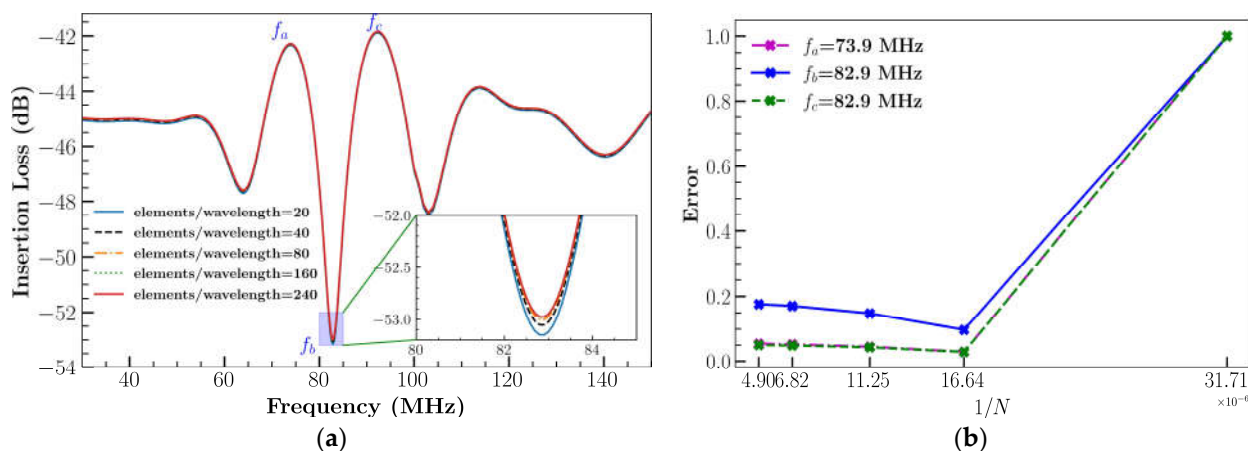


**Figure 4.** (a) Mesh sensitivity analysis; (b) error measured for 2D XY LiNbO<sub>3</sub> using different total number of elements.

The findings are shown in Figure 4a,b. The error decreases with finer mesh and absolute errors were found to be within 1% between case 2 and case 5. Case 2 was opted for the remaining simulations due to decreased computational requirements with similar error.

Further FEM analysis was extended to 3D cases with different orientations and cuts: 3D XY LiNbO<sub>3</sub>, 3D YX LiNbO<sub>3</sub> and 3D YX 128° LiNbO<sub>3</sub>. The results are illustrated in Figure 5a,b. Compared to the 2D XY cut, the 3D XY cuts of LiNbO<sub>3</sub> results were in good agreement with the experimental outcomes [26] (Figure 5a). The addition of the extra dimension (length) to the model resulted in enhanced IL, which is in good agreement with previous results [31]. However, results of IL differ at higher frequency. This could possibly be caused by the number of elements considered for IDT, the time step, the diffracted waves produced by IDT boundaries due to available computational resource limitation. This demonstrates that the wave formation in the third direction influences the device's performance. Figure 5b represents the comparison of simulation and experimental results of different orientations of LiNbO<sub>3</sub>. 3D XY cut LiNbO<sub>3</sub> model captures a better result than a 2D model in most of the frequency locations as represented in relative error comparison plot Figure 6 with the experimental result.

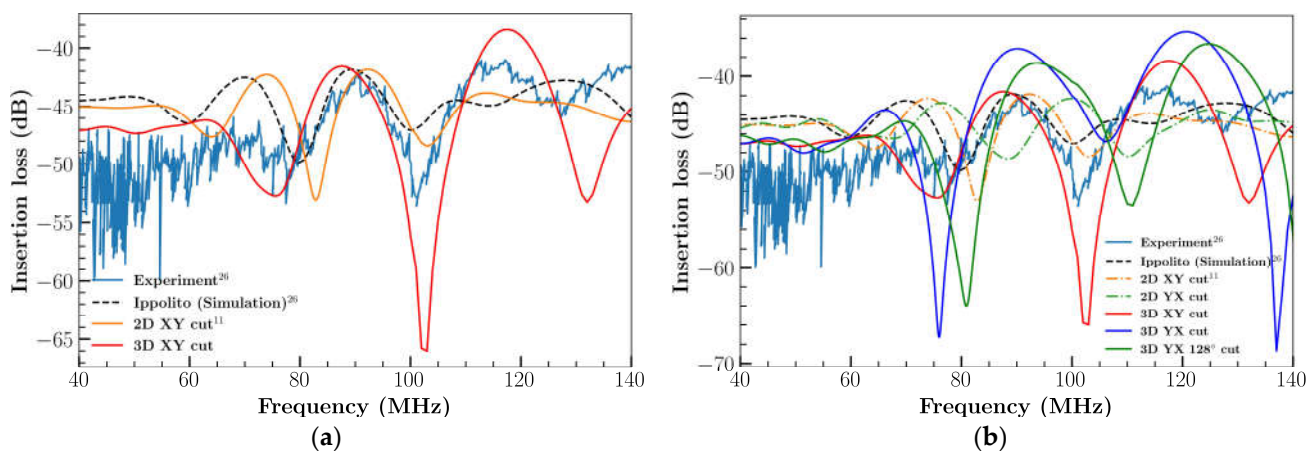


**Figure 5.** (a) Comparison of IL with experimental and simulation results; (b) comparison of IL with experimental and simulation results with different orientation of LiNbO<sub>3</sub>.

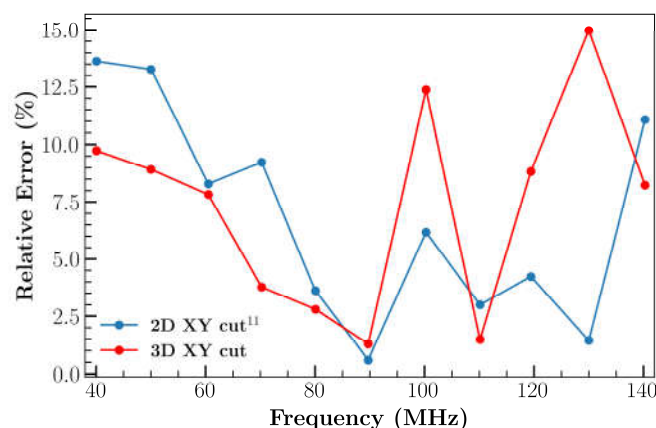


**Figure 6.** Comparison of relative error between experimental result and simulation result for 2D and 3D XY cut.

### 3.2. Characteristics of Parameters

#### 3.2.1. Thickness

A parametric study was conducted to investigate the impact of electrode thickness on IL by utilizing the 3D XY LiNbO<sub>3</sub> model. The impact of the electrode thickness on IL was represented in Figure 7a. A lower frequency shift was observed due to the increment in the thickness of the electrode. In addition, Figure 7b illustrates the relative error of IL. A significant increase in IL was determined at frequencies > 100 MHz for thick (5  $\mu\text{m}$ ) electrodes, which is believed to be due to the increased mass. A 0.5  $\mu\text{m}$  electrode thickness was selected for all future simulations due to the reduced error.

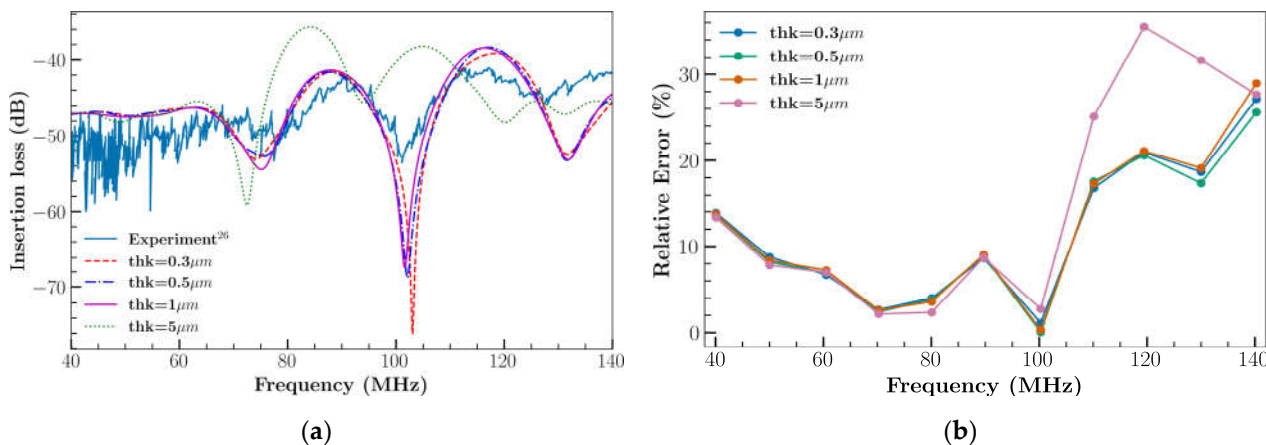


**Figure 7.** (a) Effect of electrode thickness on IL; (b) comparison of relative error between experimental result and simulation result by varying the thickness of electrode.

#### 3.2.2. 3D Model

The characteristics of the 3D XY LiNbO<sub>3</sub> model were analyzed using the impulse condition mentioned in Equation (9). Figure 8a shows the displacement components of 3D XY LiNbO<sub>3</sub> at location ( $x = 800 \mu\text{m}$ ,  $y = 200 \mu\text{m}$ ,  $z = 500 \mu\text{m}$ , Figure 2) for a duration of 100 ns. Results illustrate the effect of displacement in the  $U_z$  direction, which is normal to the propagation direction ( $U_y$ ). IL (Figure 5) was affected by the displacement of the  $U_z$  component which resulted in a good agreement with the predicted IL for the 3D XY LiNbO<sub>3</sub>. The amplitude of both  $U_x$  and  $U_y$  components were predominant at the surface and decayed along the depth of 6–8 wavelength of the device as represented in Figure 8b,c. Similar simulation outcomes for 3D model SAW devices were reported in previous studies [26,30]. Hence later simulation analysis was performed by considering the 3D model of LiNbO<sub>3</sub>.

Contour plots of deformation for 3D XY LiNbO<sub>3</sub> at different time steps are provided in the appendix section (Appendix A).

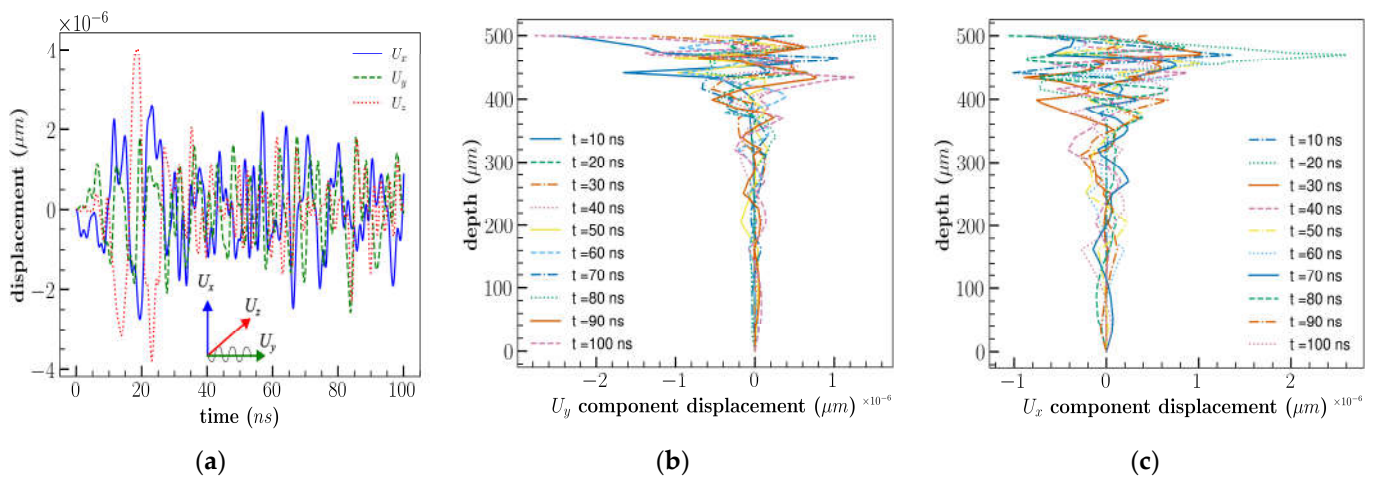


**Figure 8.** Simulation results of 3D XY LiNbO<sub>3</sub> (a) displacement components with respect to time, at location ( $x = 800 \mu\text{m}$ ,  $y = 200 \mu\text{m}$ ,  $z = 500 \mu\text{m}$ ); (b)  $U_y$ ; (c)  $U_x$  displacement component along the depth at location ( $x = 800 \mu\text{m}$ ,  $y = 200 \mu\text{m}$ ).

### 3.3. SAW

#### 3.3.1. Single Direction Travelling SAW

Different orientations of the 3D model of LiNbO<sub>3</sub>: (a) XY cut, (b) YX cut and 128<sup>o</sup> YX cut were subjected to the peak-to-peak continuous sinusoidal voltage of 1 V and frequency of 100 MHz applied at left IDT only (Figure 2). This subsection was referred to as single direction or traveling SAW (tSAW). IL and displacement components (perpendicular to propagation direction) were analyzed in the material coordinate system (X, Y, Z) and represented in Figure 9a,b at the same location (800  $\mu\text{m}$ , 200  $\mu\text{m}$ , 500  $\mu\text{m}$ ).

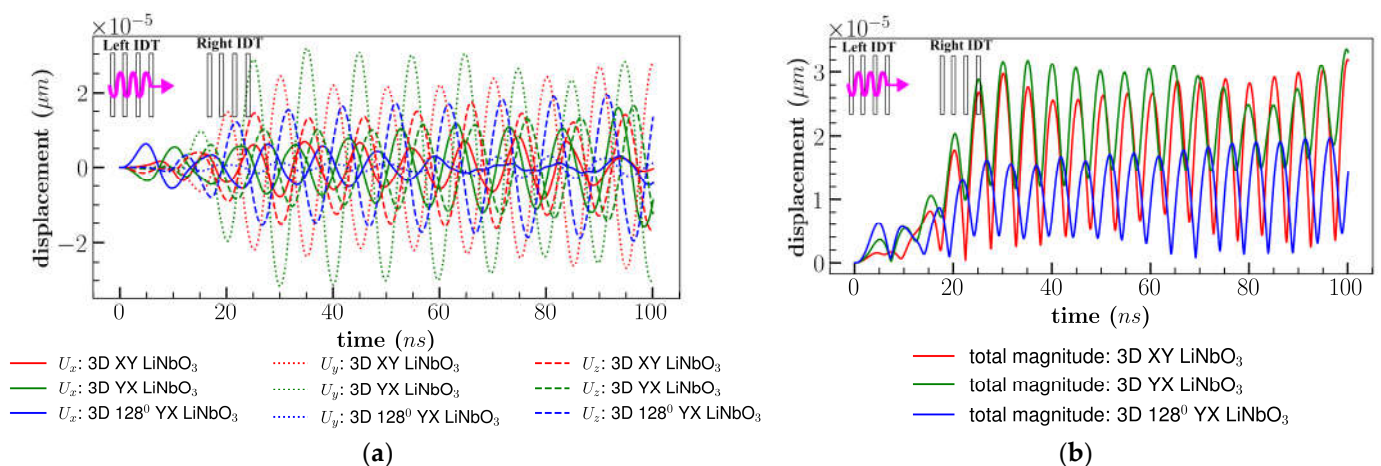


**Figure 9.** Comparison of (a) displacement components; (b) total displacement magnitude for different orientation of LiNbO<sub>3</sub> SAW for single direction.

Figure 9a indicates that the  $U_y$  displacement component was predominant for XY and YX cut LiNbO<sub>3</sub> with order of magnitude  $\sim 10^{-5} \mu\text{m}$  and least for 128<sup>o</sup> YX cut LiNbO<sub>3</sub> ( $\sim 10^{-6} \mu\text{m}$ ). The out-of-plane displacement ( $U_z$ ) which was normal to the propagation direction was found to be maximum for 128<sup>o</sup> YX cut LiNbO<sub>3</sub>. The variation in the dominance of the displacement components was due to the anisotropic property of the materials under different cuts. The impact of varying the length of the electrode on  $U_z$  component was insignificant as shown in Figure 10. However,  $U_x$  displacement component was decreased

to an average of 50% for XY cut and increased to 50% for YX cut in comparison to the design consisting of electrode length 300  $\mu\text{m}$ . Similar to XY cut, displacement component  $U_x$  was reduced for 128<sup>0</sup> YX cut with electrode length of 4500  $\mu\text{m}$ . It may be noted that the length of the electrode affects the displacement component along  $U_x$  and similar results were observed in previous studies which improved the cell separation due to the longer length of the electrode [8]. A detailed comparison of displacement components for varying electrode lengths is provided in the appendix section (Appendix A).

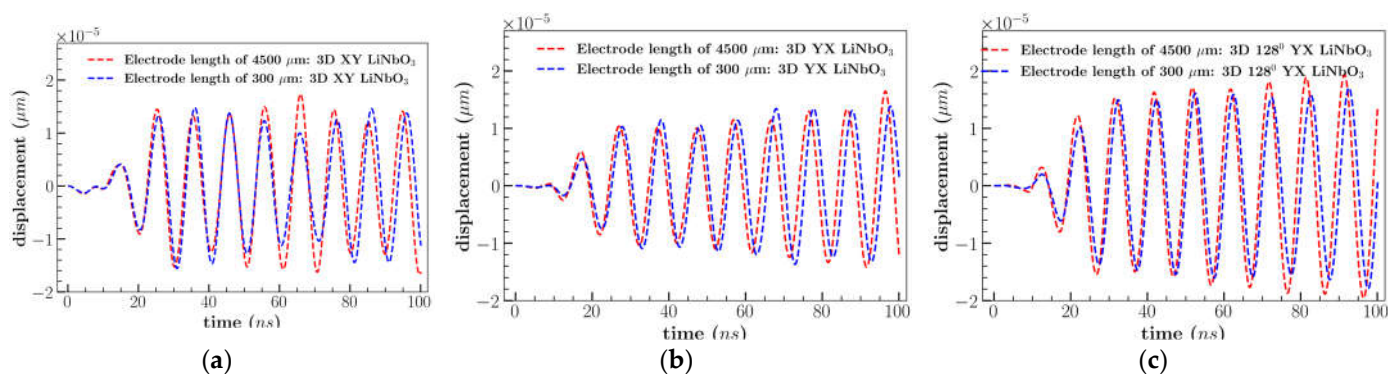


**Figure 10.** Comparison of  $U_z$  displacement for (a) XY; (b) YX; (c) 128<sup>0</sup> YX cut LiNbO<sub>3</sub> of electrode length of 4500  $\mu\text{m}$  and 300  $\mu\text{m}$ .

The total magnitude was highest for YX cut (average of  $3 \times 10^{-5}$   $\mu\text{m}$ ) due to the large displacement of the  $U_y$  component (Figure 9b). On the other hand, the 128<sup>0</sup> YX cut had the lowest total magnitude because of the low  $U_y$  component but 128<sup>0</sup> YX had the largest  $U_z$  displacement with an average peak of  $1.8 \times 10^{-5}$   $\mu\text{m}$  (Figure 10c). Figure 11 represents the comparison of IL between LiNbO<sub>3</sub> orientation. IL was found to be minimum for YX cut with a range from 22 dB to  $-66$  dB in comparison with YX cut 128<sup>0</sup> LiNbO<sub>3</sub> (range: 14 to  $-86$  dB) and XY cut LiNbO<sub>3</sub> (range: 14 to  $-65$  dB).

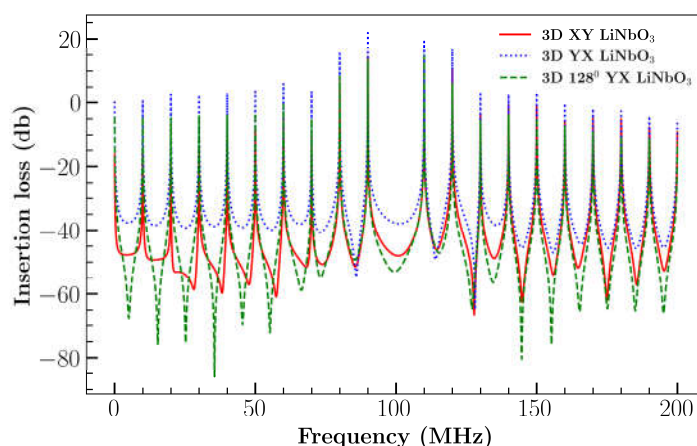


**Figure 11.** Comparison of IL for different orientations of LiNbO<sub>3</sub> for single direction.

### 3.3.2. Bi-Directional/s SAW

This section demonstrates the effect of applying the same peak-to-peak voltage to both sets of IDTs working in both directions (left and right IDT Figure 2) and visualizes the effect of interference amplitude. The vertical displacement ( $U_z$ ) of 128<sup>0</sup> YX cut LiNbO<sub>3</sub> was increased by 65–70% compared to single direction due to interference of the stationary waves as shown in Figure 12. According to the result,  $U_x$  displacement was reduced to 50% when compared to single direction case by establishing dominance in the out-of-plane direction for 128<sup>0</sup> YX cut LiNbO<sub>3</sub>. Similar effects were reported in previous experimental

investigation, demonstrating the formation of maximum out-of-plane amplitude for  $128^0$  YX cut LiNbO<sub>3</sub>, which resulted in enhanced cell separation efficiency [15].

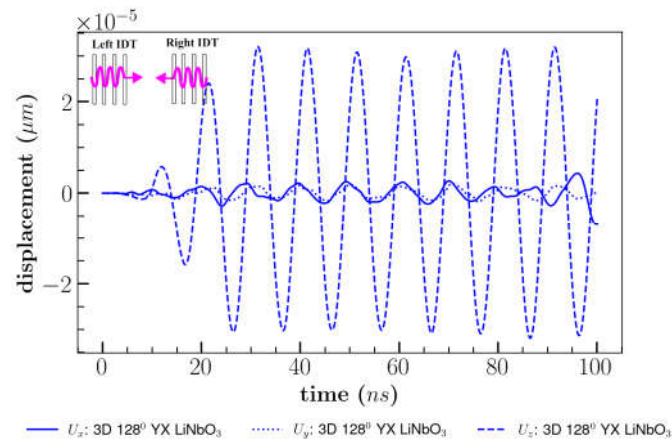


**Figure 12.** Comparison of displacements for  $128^0$  YX cut LiNbO<sub>3</sub> combining multiple waves.

Figure 13a,b represent the displacement components under sSAW for different orientations of LiNbO<sub>3</sub>. For both XY and YX cut LiNbO<sub>3</sub>, predominant displacement component  $U_y$  increased due to the constructive interference of the stationary waves. However, the amplitude of the  $U_z$  component reduced to 50% for XY cut which resembles the shear waves for XY cut LiNbO<sub>3</sub>. In contradiction,  $U_x$  component decreased for YX cut. Due to an increase in the amplitude of the dominant component, the total displacement magnitude became larger for all cuts.

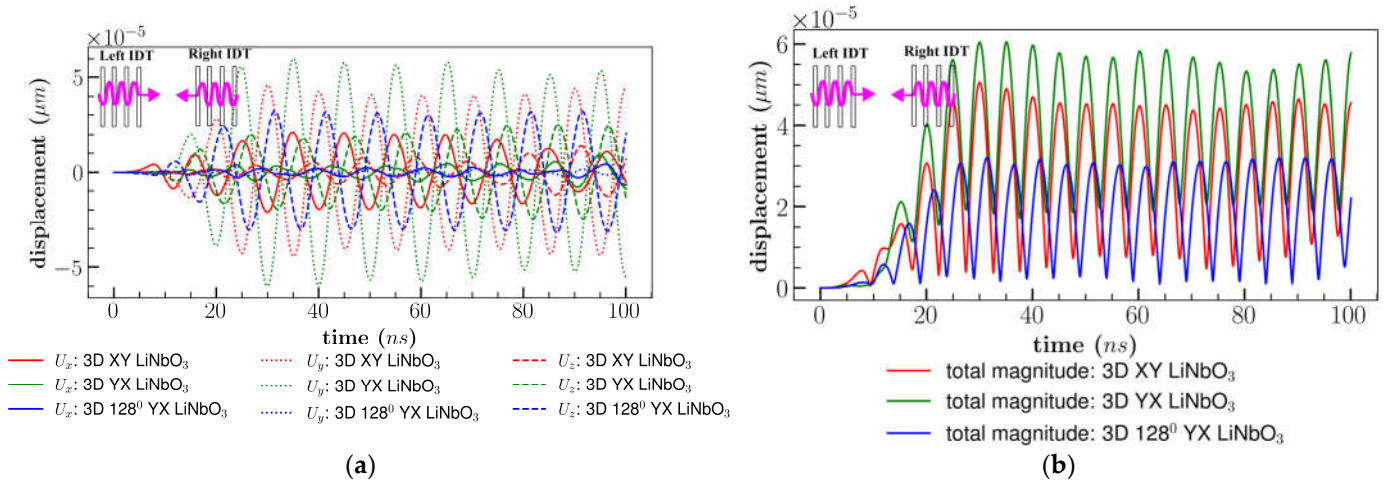


**Figure 13.** Comparison of (a) displacement components; (b) total displacement magnitude for different orientation of LiNbO<sub>3</sub> combining multiple waves.

### 3.3.3. Bi-Directional Wave Delay

We investigated the inference effects of stationary waves under the influence of peak-to-peak voltage by creating two sets of waves in opposite directions. Here, the input continuous signal was applied to the left IDT from the beginning, however, the right IDT was delayed by 50 ns. For comparison between the results of the earlier subsection, the delay input signal to the right IDT was turned on at the halfway point of the total simulation time to demonstrate its impact.

Results are depicted in Figure 14a,b by comparing the different orientations of the LiNbO<sub>3</sub>. The total displacement magnitude for all cuts were similar to a single input until 50 ns. However, delaying the right IDT, increased the amplitude of XY cut by an average of 5% and  $128^0$  YX cut by 6% after 80 ns, nonetheless, results of YX cut remain unaltered in

comparison to the bi-directional condition as represented in Figure 14b. Constructive waves generated in the active area (microfluidic channel area) did not reach a stable displacement until 30 ns after right IDT activation, but delaying the input signal enhanced the interference amplitude which led to improving the amplitude of the overall displacement after 80 ns.

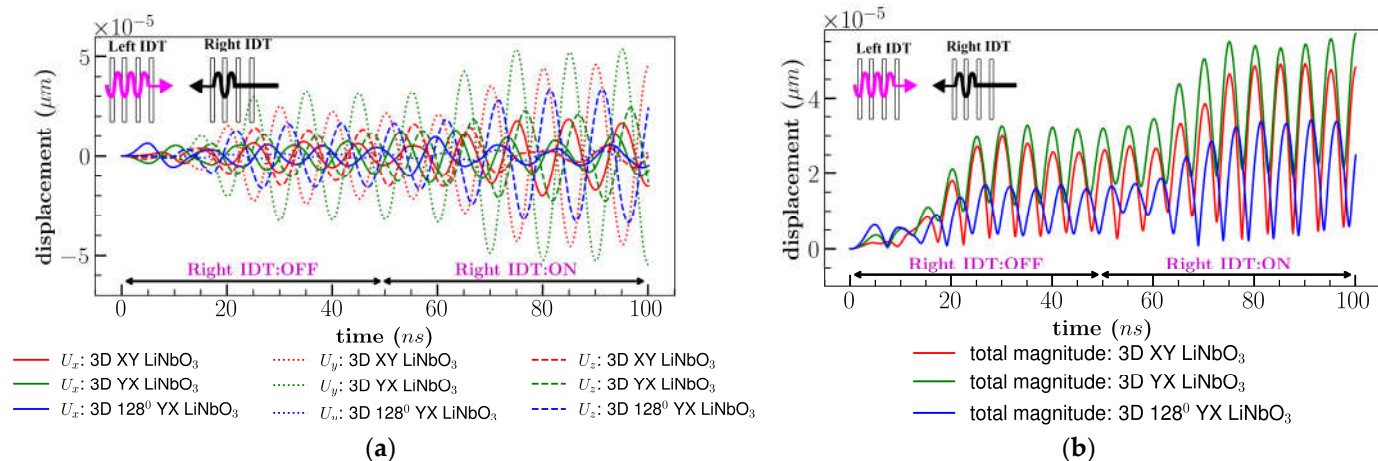


**Figure 14.** Comparison of (a) displacement components; (b) total displacement magnitude for different orientation of LiNbO<sub>3</sub> for bi-direction (wave delay).

Figure 15 represents the overall comparison for out-of-plane ( $U_z$ ) displacement of three cuts for three input signal cases: single direction, bi-direction, and bi-direction (wave delay). The maximum amplitude ( $U_z$ ) was observed to be higher for 128° YX cut in all three-input signal conditions by 50% in comparison to other cuts. Combining the multiple waves improved the out-of-plane ( $U_z$ ) displacement for 128° YX cut. However, delaying the right IDT increased the  $U_z$  displacement marginally by 6% after 80 ns. A series of plots are provided in the appendix section (Appendix A) which compares the individual displacement component for the three cases: single direction, bi-direction, and bi-direction (wave delay).

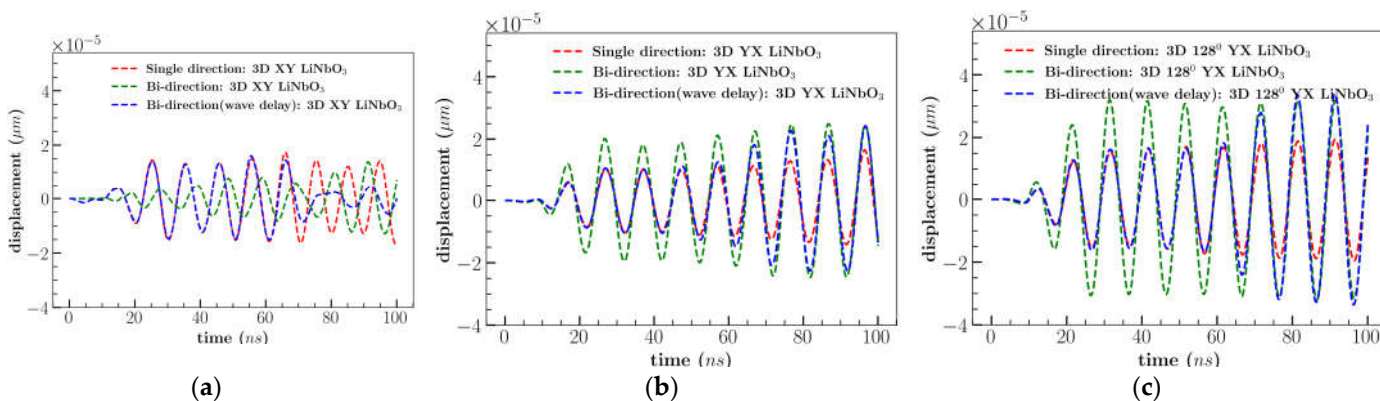


**Figure 15.** Simulation results of out-of-plane ( $U_z$ ) displacement considering cases single direction, bi-direction and bi-direction (wave delay) for (a) XY, (b) YX, and (c) 128° YX cut LiNbO<sub>3</sub>.

Overall, the 3D FEM model of XY LiNbO<sub>3</sub> performed well with experimental findings [26] in comparison to the 2D model based on the parameter IL. The characteristic investigation demonstrated that high frequency propagation waves were restricted to the surface and the thickness of the electrode affects the operating frequency of the device. According to the results of numerical analysis for single direction case, the higher significant displacement was observed in the length direction  $U_y$  (according to material coordinate system, Figure 2) for XY and YX cuts, whereas out-of-plane amplitude ( $U_z$ ) was predominated

for  $128^0$  YX cut. The length of the electrode reduced the magnitude of  $U_x$  component to 30–60% for XY and  $128^0$  YX cut while it increased for YX cut in comparison with a shorter electrode (electrode length 300  $\mu\text{m}$ ). This suggests that the length of electrode affects the other displacement components and also previous studies specified that the efficiency of cell separation based on acoustofluidics depends on the length of the electrode [8].

The combination of the multiple input signal (bi-direction) conditions increased the displacement of the predominant components for all cuts. Due to the constructive interference of the stationary waves the out-of-plane ( $U_z$ ) component was increased to 50% for  $128^0$  YX cut and a significant reduction in the displacement of the  $U_x$  and  $U_y$  component (Figure 15c). Similar observations were demonstrated in earlier studies which improved the cell separation efficiency by sSAW [15]. Wave formation in the XY cut was comparable to shear waves (inplane) with a considerable decrease in the magnitude of the  $U_z$  component by the interference of the waves. Delaying the input signal marginally improved the amplitude of the dominating component in XY and  $128^0$  YX cut whereas YX cut remained unchanged. However, the particle/cell separation efficiency of the device also depends on various aspects such as IDT design, width of the formed surface waves, microfluidic channel material and acoustic energy. Other important factors that impact cell separation are acoustic radiation and drag force induced by the acoustic streaming on the suspended particles. Cell separation due to acoustic radiation is mostly determined by particle dimensions and wavelength. The size of the particles affects both forces and previous studies [32,33] demonstrated that their relative dominance leads to the separation of the particles. The effect of these forces under the sSAW could be investigated in future work.

#### 4. Conclusions

The current work compared 2D and 3D FEM models of XY-cut  $\text{LiNbO}_3$  results with experimental data [26]. Numerical analysis findings on the high aspect ratio of length to width of IDT imply that the  $U_x$  component of the mechanical waves depends on the IDT length. Three orientations of  $\text{LiNbO}_3$ : XY cut, YX cut and  $128^0$  YX cut were analyzed under different input signal conditions (i.e., single, bi-direction and bi-direction (wave delay)) by applying a peak-to-peak voltage to the left and right IDTs. Single-direction input signal results showed that the predominance of surface waves amplitude was dependent on crystal cut. Conversely, the coherence of the multiple waves improved the predominant wave displacement by 50% reducing the other displacement components under bi-direction and wave delay conditions. Wave delay study shows that the combination of applying continuous and pulse signal requires matching of the pressure antinode and node for the enhanced displacement. Hence, device performance can be improved by adjusting the displacement components which results in altering the interference amplitude of the waves through bi-direction/sSAW. From the analysis, it was observed that  $128^0$  YX cut  $\text{LiNbO}_3$  were able to produce a higher amplitude of out-of-plane waves which would be most suitable for cell separation application based on acoustofluidics. This base FEM model can be integrated with microfluidics considering the other influential factors in subsequent work, and experiments would be conducted to further validate the model.

**Author Contributions:** Conceptualization, R.D.J. and N.J.; methodology, R.D.J. and N.J.; software, R.D.J.; validation, R.D.J.; analysis, R.D.J.; investigation, R.D.J.; resources, N.J.; data curation, R.D.J. and N.J.; writing—original draft preparation, R.D.J.; writing—review and editing, N.J.; supervision, N.J. All authors have read and agreed to the published version of the manuscript.

**Funding:** This research received no external funding.

**Institutional Review Board Statement:** Not applicable.

**Data Availability Statement:** Not applicable.

**Acknowledgments:** The authors would like to thank all members of the SMART Laboratory group at the University of New Mexico.

**Conflicts of Interest:** The authors declare no conflict of interest.

### Appendix A. Additional Simulation Results

#### Appendix A.1. Deformation Contour of 3D Model for Electrode Length 4500 $\mu\text{m}$

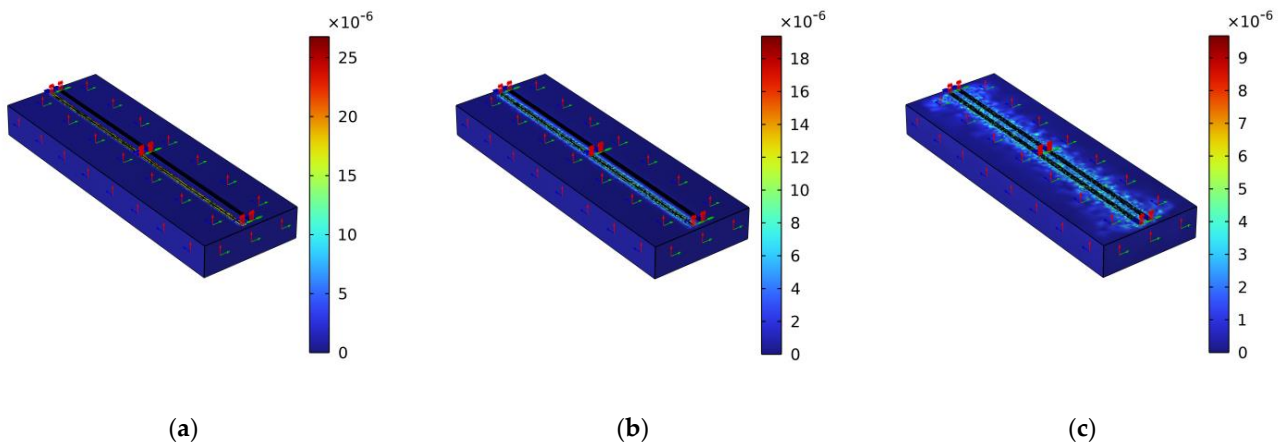


**Figure A1.** Simulation results of 3D XY LiNbO<sub>3</sub> on (a)  $t = 1$  ns; (b)  $t = 10$  ns; (c)  $t = 100$  ns.

#### Appendix A.2. Deformation Contour for Electrode Length 4500 $\mu\text{m}$ : Single Direction

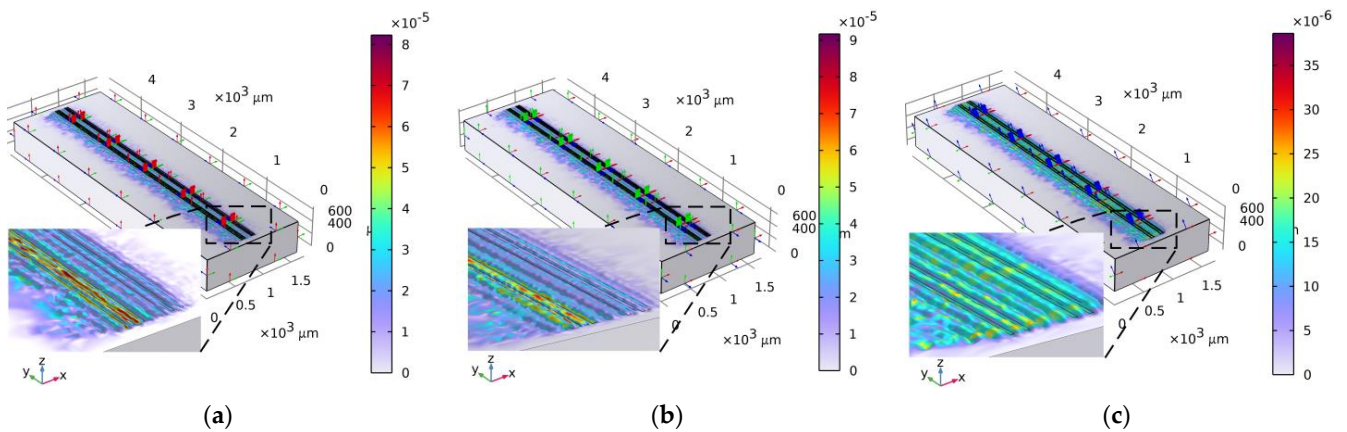


**Figure A2.** Contour plot of deformation with crystal orientations for (a) XY; (b) YX; (c)  $128^0$  YX cut LiNbO<sub>3</sub> single direction.

#### Appendix A.3. Deformation Contour for Electrode Length 4500 $\mu\text{m}$ : Bi-Direction

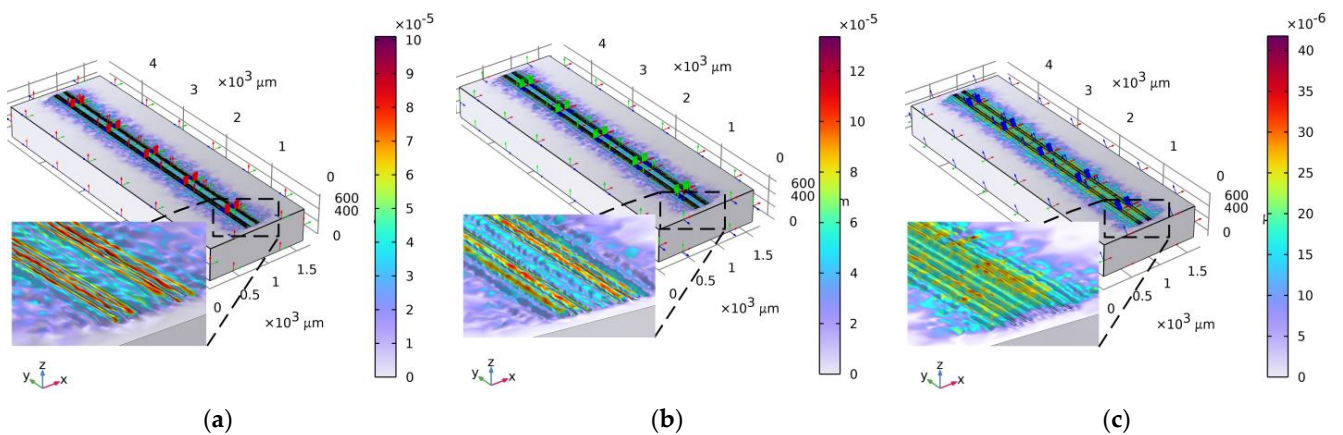


**Figure A3.** Contour plot of deformation with crystal orientations for (a) XY; (b) YX; (c)  $128^0$  YX cut LiNbO<sub>3</sub>: Bi-direction.

#### Appendix A.4. Deformation Contour for Electrode Length 300 $\mu\text{m}$ : Single Direction

The computational domain for shorter length electrode was chosen with overall dimensions  $1600 \mu\text{m} \times 500 \mu\text{m} \times 500 \mu\text{m}$ . The length of the electrode was considered as  $300 \mu\text{m}$  (shorter) with thickness and width of  $0.5 \mu\text{m}$  and  $10 \mu\text{m}$  respectively.

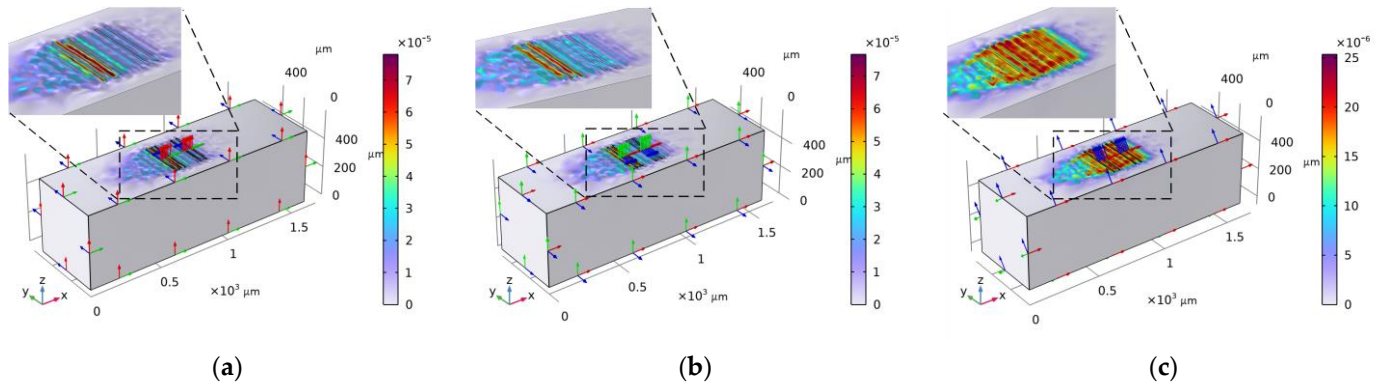


**Figure A4.** Contour plot of deformation with crystal orientations for (a) XY; (b) YX; (c)  $128^\circ$  YX cut  $\text{LiNbO}_3$ : Bi direction.

#### Appendix A.5. Comparison of Displacement Components for Electrode Length 300 $\mu\text{m}$ and Length 4500 $\mu\text{m}$ : Single Direction

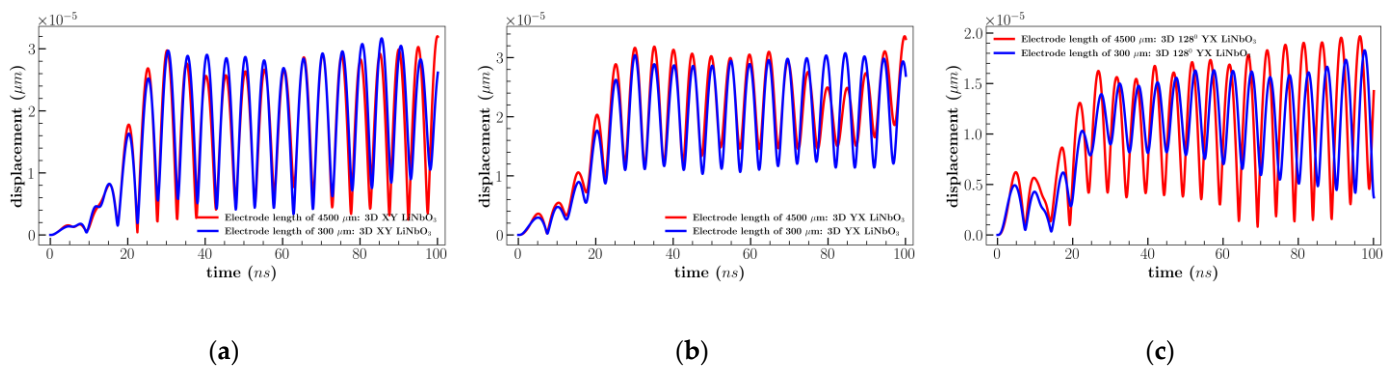


**Figure A5.** Simulation results of total displacement for (a) XY; (b) YX; (c)  $128^\circ$  YX cut  $\text{LiNbO}_3$ .

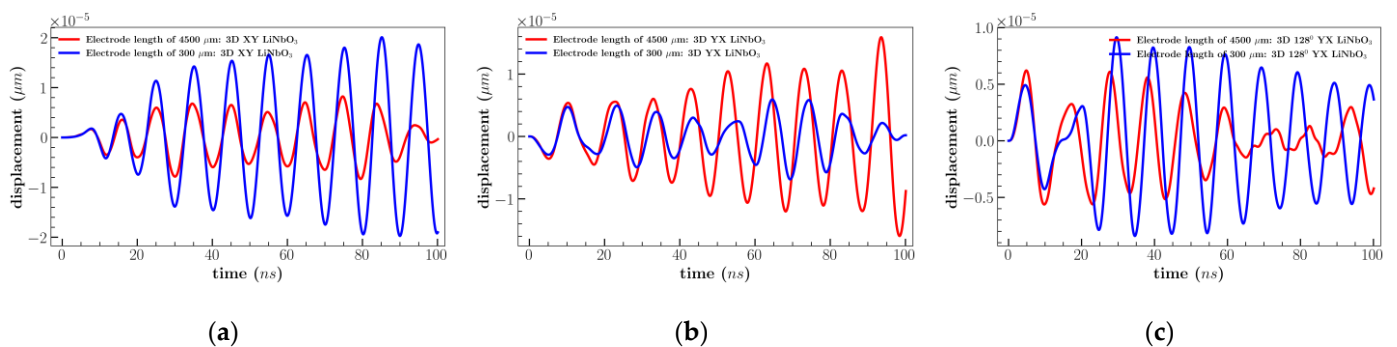


**Figure A6.** Simulation results for  $U_x$  displacement for (a) XY; (b) YX; (c)  $128^\circ$  YX cut  $\text{LiNbO}_3$ .

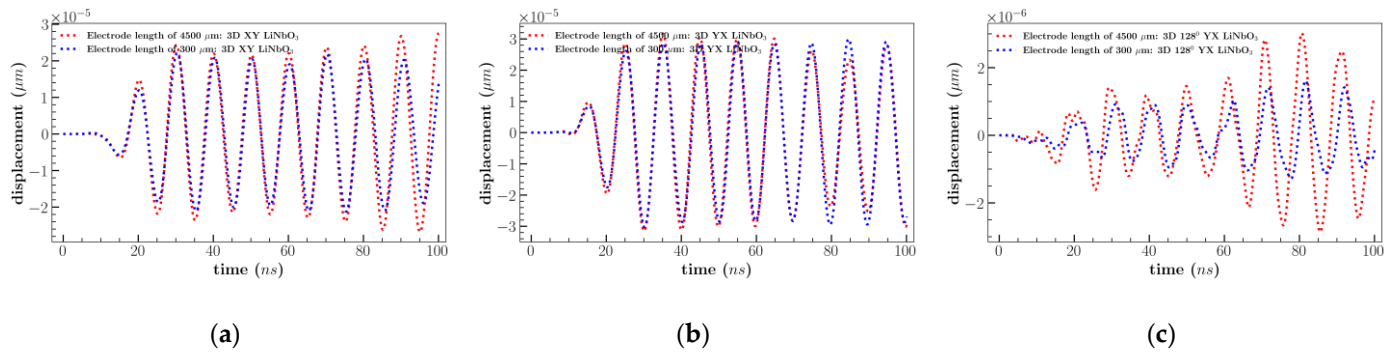


**Figure A7.** Simulation results for  $U_y$  displacement for (a) XY; (b) YX; (c)  $128^\circ$  YX cut LiNbO<sub>3</sub>.

*Appendix A.6. Comparison of Displacement Components under Single Direction, bi-Direction and bi-Direction (Wave Delay) for Electrode Length 4500  $\mu\text{m}$*

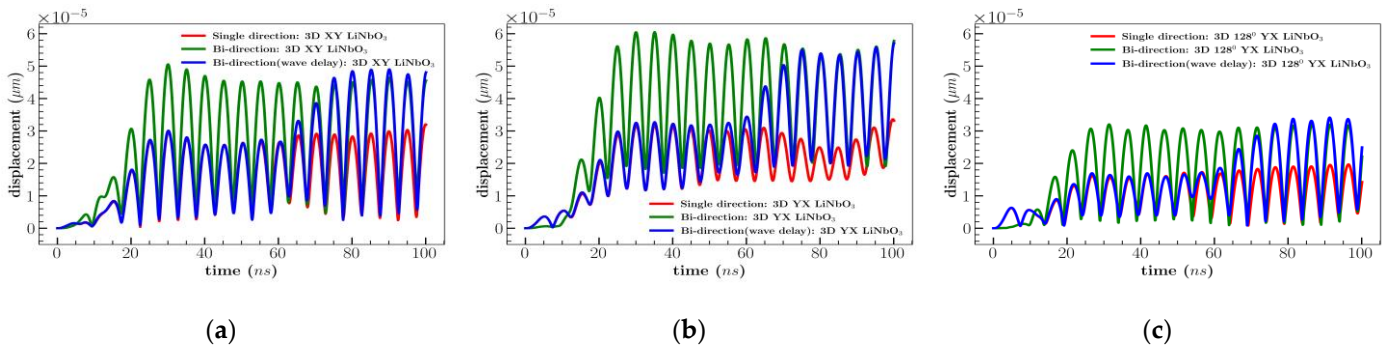


**Figure A8.** Simulation results of for total displacement for (a) XY; (b) YX; (c)  $128^\circ$  YX cut LiNbO<sub>3</sub>.

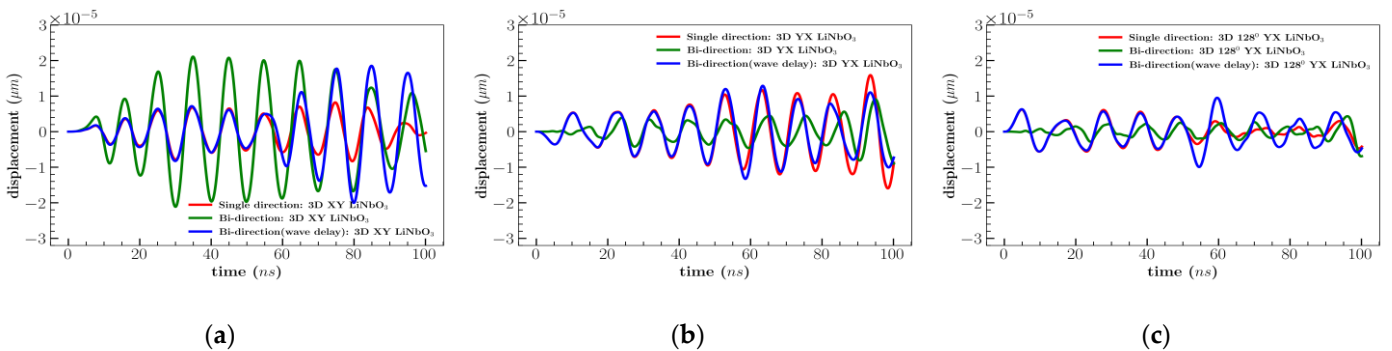


**Figure A9.** Simulation results for  $U_x$  displacement for (a) XY; (b) YX; (c)  $128^\circ$  YX cut LiNbO<sub>3</sub>.

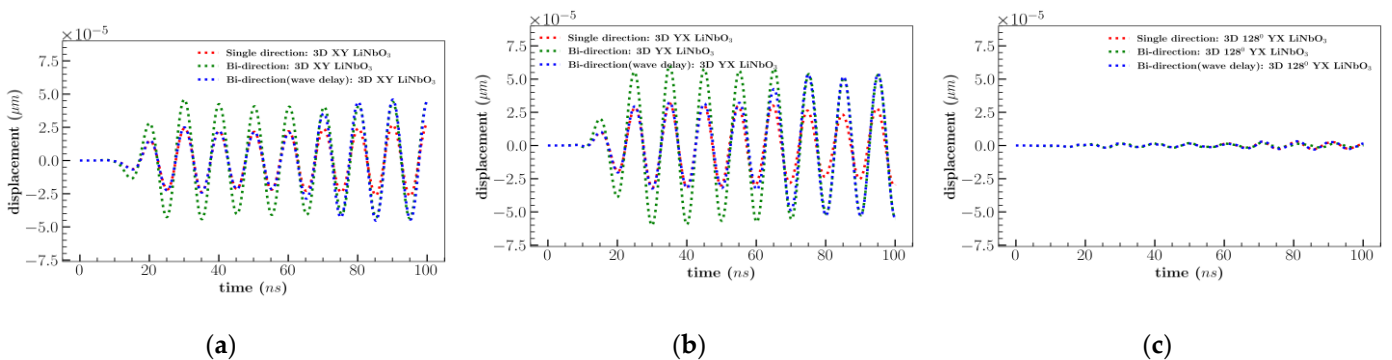


**Figure A10.** Simulation results for  $U_y$  displacement for (a) XY; (b) YX; (c)  $128^\circ$  YX cut LiNbO<sub>3</sub>.

## References

1. Rufo, J.; Cai, F.; Friend, J.; Wiklund, M.; Huang, T.J. Acoustofluidics for Biomedical Applications. *Nat. Rev. Methods Primers* **2022**, *2*, 30. [CrossRef]
2. Destgeer, G.; Sung, H.J. Recent Advances in Microfluidic Actuation and Micro-Object Manipulation via Surface Acoustic Waves. *Lab Chip* **2015**, *15*, 2722–2738. [CrossRef]
3. Winkler, A.; Bergelt, P.; Hillemann, L.; Menzel, S. Influence of Viscosity in Fluid Atomization with Surface Acoustic Waves. *OJA* **2016**, *6*, 23–33. [CrossRef]
4. Wu, M.; Ouyang, Y.; Wang, Z.; Zhang, R.; Huang, P.-H.; Chen, C.; Li, H.; Li, P.; Quinn, D.; Dao, M.; et al. Isolation of Exosomes from Whole Blood by Integrating Acoustics and Microfluidics. *Proc. Natl. Acad. Sci. USA* **2017**, *114*, 10584–10589. [CrossRef] [PubMed]
5. Zhang, S.P.; Lata, J.; Chen, C.; Mai, J.; Guo, F.; Tian, Z.; Ren, L.; Mao, Z.; Huang, P.-H.; Li, P.; et al. Digital Acoustofluidics Enables Contactless and Programmable Liquid Handling. *Nat. Commun.* **2018**, *9*, 2928. [CrossRef]
6. Togami, Y.; Chiba, T. Observation of Bulk Waves and Surface Waves through Side Planes of Several Cuts of LiNbO<sub>3</sub> SAW Devices. *J. Appl. Phys.* **1978**, *49*, 3587–3589. [CrossRef]
7. Namnabat, M.S.; Moghimi Zand, M.; Houshfar, E. 3D Numerical Simulation of Acoustophoretic Motion Induced by Boundary-Driven Acoustic Streaming in Standing Surface Acoustic Wave Microfluidics. *Sci. Rep.* **2021**, *11*, 13326. [CrossRef]
8. Li, P.; Mao, Z.; Peng, Z.; Zhou, L.; Chen, Y.; Huang, P.-H.; Truica, C.I.; Drabick, J.J.; El-Deiry, W.S.; Dao, M.; et al. Acoustic Separation of Circulating Tumor Cells. *Proc. Natl. Acad. Sci. USA* **2015**, *112*, 4970–4975. [CrossRef]
9. Wu, M.; Ozcelik, A.; Rufo, J.; Wang, Z.; Fang, R.; Jun Huang, T. Acoustofluidic Separation of Cells and Particles. *Microsyst. Nanoeng.* **2019**, *5*, 32. [CrossRef]
10. Connacher, W.; Zhang, N.; Huang, A.; Mei, J.; Zhang, S.; Gopesh, T.; Friend, J. Micro/Nano Acoustofluidics: Materials, Phenomena, Design, Devices, and Applications. *Lab Chip* **2018**, *18*, 1952–1996. [CrossRef]
11. Janardhana, R.D.; Jackson, N. Characteristics of Input Signal of a XY and YX Cut LiNbO<sub>3</sub> Saw Using Finite Element Modeling. In Proceedings of the ASME International Mechanical Engineering Congress and Exposition, New Orleans, LA, USA, 29 October–2 November 2023.
12. Ding, X.; Lin, S.-C.S.; Kiraly, B.; Yue, H.; Li, S.; Chiang, I.-K.; Shi, J.; Benkovic, S.J.; Huang, T.J. On-Chip Manipulation of Single Microparticles, Cells, and Organisms Using Surface Acoustic Waves. *Proc. Natl. Acad. Sci. USA* **2012**, *109*, 11105–11109. [CrossRef] [PubMed]
13. Ren, L.; Yang, S.; Zhang, P.; Qu, Z.; Mao, Z.; Huang, P.; Chen, Y.; Wu, M.; Wang, L.; Li, P.; et al. Standing Surface Acoustic Wave (SSAW)-Based Fluorescence-Activated Cell Sorter. *Small* **2018**, *14*, 1801996. [CrossRef]
14. Li, S.; Ding, X.; Guo, F.; Chen, Y.; Lapsley, M.I.; Lin, S.-C.S.; Wang, L.; McCoy, J.P.; Cameron, C.E.; Huang, T.J. An On-Chip, Multichannel Droplet Sorter Using Standing Surface Acoustic Waves. *Anal. Chem.* **2013**, *85*, 5468–5474. [CrossRef] [PubMed]
15. Shi, J.; Mao, X.; Ahmed, D.; Colletti, A.; Huang, T.J. Focusing Microparticles in a Microfluidic Channel with Standing Surface Acoustic Waves (SSAW). *Lab Chip* **2008**, *8*, 221–223. [CrossRef]
16. Ding, X.; Shi, J.; Lin, S.-C.S.; Yazdi, S.; Kiraly, B.; Huang, T.J. Tunable Patterning of Microparticles and Cells Using Standing Surface Acoustic Waves. *Lab Chip* **2012**, *12*, 2491. [CrossRef] [PubMed]
17. Lv, H.; Chen, X.; Zhang, Y.; Wang, X.; Zeng, X.; Zhang, D. Two-stage Particle Separation Channel Based on Standing Surface Acoustic Wave. *J. Microsc.* **2022**, *286*, 42–54. [CrossRef]
18. Ni, Z.; Yin, C.; Xu, G.; Xie, L.; Huang, J.; Liu, S.; Tu, J.; Guo, X.; Zhang, D. Modelling of SAW-PDMS Acoustofluidics: Physical Fields and Particle Motions Influenced by Different Descriptions of the PDMS Domain. *Lab Chip* **2019**, *19*, 2728–2740. [CrossRef]
19. Hsu, J.-C.; Chao, C.-L. Full-Wave Modeling of Micro-Acoustofluidic Devices Driven by Standing Surface Acoustic Waves for Microparticle Acoustophoresis. *J. Appl. Phys.* **2020**, *128*, 124502. [CrossRef]
20. Skov, N.R.; Sehgal, P.; Kirby, B.J.; Bruus, H. Three-Dimensional Numerical Modeling of Surface-Acoustic-Wave Devices: Acoustophoresis of Micro- and Nanoparticles Including Streaming. *Phys. Rev. Appl.* **2019**, *12*, 044028. [CrossRef]
21. COMSOL Multiphysics®, v. 6.1. COMSOL, Inc. Available online: <https://cn.comsol.com/> (accessed on 3 October 2023).
22. Ballantine, D.; White, R.; Martin, S.; Ricco, A.; Zellers, E.; Frye, G.; Wohljen, H. *Acoustic Wave Sensors: Theory, Design, and Physico-Chemical Applications*; Applications of Modern Acoustics Series; Academic Press: San Diego, CA, USA, 1997; ISBN 978-0-12-077460-9.
23. Xu, G.; Jiang, Q. A Finite Element Analysis of Second Order Effects on the Frequency Response of a SAW Device. *J. Intell. Mater. Syst. Struct.* **2001**, *12*, 69–77. [CrossRef]
24. Morgan, D.P. *Surface Acoustic Wave Filters: With Applications to Electronic Communications and Signal Processing*, 2nd ed.; Academic Press: Amsterdam, The Netherlands; London, UK, 2007; ISBN 978-0-12-372537-0.
25. Reddy, J.N. *Introduction to the Finite Element Method*, 4th ed.; McGraw Hill Education: New York, NY, USA, 2019; ISBN 978-1-259-86190-1.
26. Ippolito, S.J. Investigation of Multilayered Surface Acoustic Wave Devices for Gas Sensing Applications: Employing Piezoelectric Intermediate and Nanocrystalline Metal Oxide Sensitive Layers. Ph.D. Thesis, RMIT University, Melbourne, Australia, 2006.
27. Kabir, K.M.M.; Matthews, G.I.; Sabri, Y.M.; Russo, S.P.; Ippolito, S.J.; Bhargava, S.K. Development and Experimental Verification of a Finite Element Method for Accurate Analysis of a Surface Acoustic Wave Device. *Smart Mater. Struct.* **2016**, *25*, 035040. [CrossRef]

28. Datta, S. Piezoelectric Materials: Crystal Orientation and Poling Direction. *COMSOL Blog*. Available online: <https://www.comsol.com/blogs/piezoelectric-materials-crystal-orientation-poling-direction/> (accessed on 3 October 2023).
29. Xu, G. Direct Finite-Element Analysis of the Frequency Response of a Y-Z Lithium Niobate SAW Filter. *Smart Mater. Struct.* **2000**, *9*, 973–980. [[CrossRef](#)]
30. Rao, Y.L. Nanostructure-Enhanced Surface Acoustic Love Wave Devices for Biosensing Applications. Ph.D. Thesis, University of Georgia, Athens, GA, USA, 2008.
31. Ippolito, S.J.; Kalantar-Zadeh, K.; Powell, D.A.; Wlodarski, W. A 3-Dimensional Finite Element Approach for Simulating Acoustic Wave Propagation in Layered SAW Devices. In Proceedings of the IEEE Symposium on Ultrasonics, Honolulu, HI, USA, 5–8 October 2003; pp. 303–306.
32. Fakhfouri, A.; Colditz, M.; Devendran, C.; Ivanova, K.; Jacob, S.; Neild, A.; Winkler, A. Fully Microfabricated Surface Acoustic Wave Tweezer for Collection of Submicron Particles and Human Blood Cells. *ACS Appl. Mater. Interfaces* **2023**, *15*, 24023–24033. [[CrossRef](#)] [[PubMed](#)]
33. Fan, Y.; Wang, X.; Ren, J.; Lin, F.; Wu, J. Recent Advances in Acoustofluidic Separation Technology in Biology. *Microsyst. Nanoeng.* **2022**, *8*, 94. [[CrossRef](#)] [[PubMed](#)]

**Disclaimer/Publisher’s Note:** The statements, opinions and data contained in all publications are solely those of the individual author(s) and contributor(s) and not of MDPI and/or the editor(s). MDPI and/or the editor(s) disclaim responsibility for any injury to people or property resulting from any ideas, methods, instructions or products referred to in the content.